Photoelectrochemical degradation of methylene blue dye under visible light irradiation using EG/Ag-ZrO₂ nanocomposite electrodes

Onoyivwe Monday Ama[1,2], Anku William Wilson[3,], Suprakas Sinha Ray[1,2]*

[1] Department of Chemical Sciences, University of Johannesburg, Doornfontein, 2028, Johannesburg, South Africa.
[2] DST-CSIR National Center for Nanostructured Materials, Council for Scientific and Industrial Research, Pretoria 0001, South Africa.
[3] CSIR- Water Research Institute, P. O. Box M.32, Accra, Ghana.
[*]E-mail: onoyivwe4real@gmail.com

The present study reports the application of three electrodes, consisting of exfoliated graphite (EG), EG and zirconium oxide (EG-ZrO₂), and EG and silver-doped zirconium oxide (EG/Ag-ZrO₂) in a comparative photoelectrochemical degradation of methylene blue (MB) dye in water under visible light irradiation. The Ag-ZrO₂ is prepared using a sol-gel method and used in the fabrication of EG/Ag-ZrO₂ electrodes via a wet solution method. The morphologies, crystalline structures, and surface/physicochemical properties of the nanocomposites are characterized by SEM, TEM, XRD, and UV-Vis, FTIR, and Raman spectroscopies. The SEM results show that ZrO₂ and Ag-ZrO₂ are evenly dispersed on the surfaces of EG. The XRD and Raman analyses reveal that ZrO₂ exists in the tetragonal phase. The modification of ZrO₂ with EG and Ag results in electrodes with strong absorption in the visible light region. All fabricated electrodes display the capacity to degrade MB, with EG/Ag-ZrO₂ exhibiting the highest degradation efficiency and EG the lowest. The electrode with the highest efficiency (EG/Ag-ZrO₂) is used in optimization studies, which identify the optimum conditions required for maximizing the efficiency of the degradation process. In addition, the EG/Ag-ZrO₂ is used in the degradation of MB via photolysis, as well as electrochemical and photoelectrochemical methods. The photoelectrochemical method exhibits superior performance when compared to photolysis and photocatalytic methods in the degradation of MB. The synergistic effects of Ag and ZrO₂ enhance the efficiency of EG/Ag-ZrO₂ toward the degradation of MB.

1. INTRODUCTION

Synthetic dyes have considerable commercial significance and are widely used in different industries, including the paper, leather, and textile industries [1, 2]. As a consequence, wastewater

emanating from these industries can contain large quantities of a variety of dyes (e.g., methylene blue and methyl orange). The presence of these dyes in the environment is a matter of great concern since most of them are toxic and pose therefore a serious threat to both aquatic life and human health [3–5]. Even at low concentration, these dyes change the colour of the receiving water body. This phenomenon affects the photosynthetic processes in the water adversely, disturbing thus aquatic ecosystems [6, 7]. Industrial wastewater polluted with toxic dyes must, therefore, be treated prior to its final release into the environment.

To date, a number of conventional water treatment technologies, including chemical precipitation, adsorption, and chemical oxidation, have been adopted, albeit with minimal success as far as their industrial application is concerned [3]. These treatment methods either end up causing secondary pollution or are extremely capital intensive [8]. Therefore, there is an urgent need for more economical and effective methods to replace conventional water treatment methods. The efforts directed at resolving the above-mentioned problems have led to the development of photocatalytic oxidation [9–11] and electrochemical oxidation [12–14] methods, which are considered to be more effective in the conversion of organic pollutants to carbon dioxide and water [15]. However, these methods are also associated with certain inherent limitations. The photocatalytic oxidation method, for example, suffers from rapid recombination of the photogenerated electrons and holes, which are responsible for the initiation of the pollutant degradation process [4]. In addition, as a result of the large band gap that is characteristic for most of the photocatalysts used in this process, the photocatalytic degradation of the pollutants tends to occur under ultraviolet (UV) light instead of the more abundant visible light [16–18]. By contrast, direct electrochemical degradation of the pollutants is a slow process, and the degradation of dye molecules requires the application of high current densities [19].

One of the possible ways to improve the overall efficiencies of the described methods is to enhance their visible light activities and reduce the recombination rates of the electrons and holes. These objectives can be achieved by the doping of wide-band-gap metal oxides such as zirconium oxide (ZrO_2) with metals such as silver [15]. The metal dopants capture the photogenerated electrons and prevent them from recombining with the holes [20, 21]. Ag has been identified as one of the metal dopants capable of acting as an electron acceptor in the host material and has been reported to alter positively the optical and electrical properties of the host material [22, 23]. Silver can trap the electrons from ZrO_2, thus leaving the holes free to participate in the degradation process [11]. Another method for achieving the described objectives involves the use of exfoliated graphite (EG) [24]. EG is a low-density conductive carbon material with a large specific surface area, high flexibility, profound electrical conductivity, and the ability to withstand aggressive media [25]. EG can be loaded with a photoactive metal oxide catalyst to serve as an appropriate anode for an effective electrochemical degradation process [26, 27]. ZrO_2 is a photoactive metal oxide catalyst with a significant content of oxygen vacancies, whose wide band gap can be reduced by doping with Ag. In addition, ZrO_2 possess high mechanical, thermal, chemical and photocatalytic stability [28, 29], and can, therefore, be combined with the EG to serve as an anode in photoelectrochemical processes.

The combination of photocatalytic and electrochemical methods to afford a holistic photoelectrochemical degradation method has also been proposed and represents one of the most effective means of attaining the degradation of dye pollutants [30–32]. The synergistic effect of the two

processes is known to suppress the drawbacks of the individual methods and produce outstanding results [33].

The motive of this work was to investigate the photoelectrochemical degradation of methylene blue (MB) dye using a nanocomposite electrode consisting of EG and Ag-doped ZrO_2. The degradation of MB was also done by photolysis and electrochemical methods. The results were compared with those achieved via the photoelectrochemical method. Finally, optimization studies were performed to detect the optimal settings for maximizing the efficiency of the degradation process.

2. EXPERIMENTAL

2.1 Materials and methods

All the chemicals used in this study, namely, silver nitrate ($AgNO_3$), zirconium nitrate [$Zr(NO_3)_4$], nitric acid (HNO_3), ethylene glycol, 25% aqueous ammonium solution (NH_4OH), natural graphite flakes, sulfuric acid (H_2SO_4), and MB dye were procured from Sigma-Aldrich (South Africa). A standard solution of the MB dye was prepared by dissolving the appropriate mass of the dye in deionized water (1000 mL). The desired dye concentration (20 mg/L) was obtained by diluting the standard solution.

2.2 Synthesis of Ag-doped ZrO_2 (Ag-ZrO_2)

The Ag-ZrO_2 nanoparticles were synthesized using a simple sol-gel method at 60 °C. Specifically, 0.05 g of silver nitrate was poured into deionized water (400 mL). The mixture was stirred until the solid became completely dissolved. Separately, 1 g of $Zr(NO_3)_4$ was dissolved in a beaker containing 10 mL of 0.1 M HNO_3 and the solution was stirred for 30 min. $AgNO_3$ solution and 0.6 mL of ethylene glycol were added sequentially in a dropwise manner. The ensuing solution was stirred for 1 h after which the pH was adjusted to 7.5 using 25% ammonium solution leading to the formation of an Ag-ZrO_2 precipitate. The solution was stirred for further 30 min before the reaction was stopped. The precipitate was separated by centrifugation (500 rpm), oven dried at room temperature, calcined at 500 °C, and pulverized to obtain the powdered Ag-ZrO_2 nanoparticles.

2.3 Synthesis of EG

Natural graphite (20 g) was soaked in H_2SO_4: HNO_3 (3:1, v/v) mixture overnight. The material was subsequently washed with copious amounts of deionized water until pH 7 was attained. The resultant material (graphite intercalated compound, GIC) was oven dried at 100 °C for 12 h and heated in an electric furnace at 800 °C for about 1 min. The thermal treatment disrupted the intercalation in the graphite lattice, producing ruptured graphite layers. This procedure afforded a puffed material referred to as EG.

2.4 Fabrication of composite electrodes

In order to synthesize the EG/Ag-ZrO$_2$ electrode, the EG was first dispersed in deionized water in a 1:1 ratio forming a mixture which was continuously stirred for 12 h and subsequently subjected to 6 h of sonication. The Ag-ZrO$_2$ (1 g) was mixed with the dispersed EG. The mixture was sonicated for another 4 h, oven dried for 6 h at 100 °C. The EG/Ag-ZrO$_2$ nanocomposites were pelleted and used to produce the electrode. The EG and EG-ZrO$_2$ electrodes were also fabricated following this procedure.

2.5. Characterization

The surface morphologies of the samples were studied using scanning electron microscopy (SEM). Details of the elemental compositions of the samples were obtained using energy dispersive X-ray spectrometer (EDS) attached to the SEM. Surface area, pore size, and pore volume information were acquired through the use of micromeritics Trista II surface area and porosity analyzer. The optical properties were examined via UV-Vis absorbance and diffuse reflectance spectroscopy studies using dry powders with LAMBDA 750 Perkin Elmer as the internal standard. The X-ray diffraction (XRD) patterns were obtained through the use of an X'PERT PRO Wide ANGLE diffractometer with Cu-kα radiation. The XRD data were used to identify the crystallinities, phases, and particles sizes of the composites. Raman spectroscopy analysis was performed using a Raman spectroscope.

2.6. Photoelectrochemical degradation experiments

The photoelectrochemical degradation of MB dye was executed in a 100 mL photoreactor using each of the fabricated materials (EG, EG/ZrO$_2$, and EG/Ag-ZrO$_2$) with the same surface area of 0.7855 cm^2 as the working electrodes. Ag/AgCl (3.0 M KCl) was used as the reference electrode, while a platinum foil was used as the counter electrode. The power requirements of the degradation experiment were met using a potentiostat that provided voltage and current ranges of 1–3 V and 7.5–15 mA, respectively. A solar simulator (250 W) fitted with a UV filter was used to provide the visible light for the experiment. A 100 mL of an aqueous solution containing MB dye at a concentration of 20 mg/L in a 0.1 M Na$_2$SO$_4$ supporting electrode was poured into the reactor, and the electrodes were connected to the electrochemical instrument. The system was switched on and the degradation experiment was performed for 4 h under continuous magnetic stirring. Aliquots of the dye under degradation (5 mL) were withdrawn from the reactor every 30 min and the concentration of the dye remaining in each sample was determined using UV-Vis spectroscopy. The effects of the solution pH, current density, and applied potential on the degradation efficiencies of the electrodes were also investigated.

2.7. HPLC analysis

The test samples (dye degradation products, 1mL) were taken at specific time intervals (15 min) and analysed using HPLC-photodiode array detector (UltiMate 3000). The pollutant degradation was

monitored at 225 nm. Elution of the samples was achieved by a gradient method at a 0.2 mL min^{-1} flow rate using a Phenomenex LUNA 5 mm C18 reversed phase column (150 x 4.60 mm). Initially, the sample was eluted for 6 min using 70 % ultra-pure water and 30 % acetonitrile. Subsequently, the acetonitrile's ratio was increased within 2 min from 30% to 90 % and held for 1 min. The ratio was then reduced back to 30 % within 8 min and was held constant for 3 min. Analysis of the intermediates products was achieved using LC/MS/MS. They were separated using an LC-20Ad XR model liquid chromatography (LC). The column and the mobile phase used in the LC were the same as those used in the HPLC analysis.

3. RESULT AND DISCUSSIONS

3.1. SEM, TEM and EDX Analysis

Figures 1a to 1c show the SEM images of EG, EG-ZrO$_2$, and EG/Ag-ZrO$_2$ nanocomposites, respectively. Natural graphite exhibits an ordered structure, however, in the EG (Figure 1a), the structure has become raptured. Figures 1b and 1c show the surface of the EG visibly modified with ZrO$_2$ Ag-ZrO$_2$ nanoparticles, respectively. The ZrO$_2$ and Ag-ZrO$_2$ particles are observed as white particles, uniformly distributed on the EG surface. Figure 3d shows the TEM image of the evenly distributed Ag-ZrO$_2$ nanoparticles. As observed in Figure 1c, the TEM image of EG/Ag-ZrO$_2$ nanocomposites (Fig 1e) reveals that the surface of the EG is modified/covered with EG/Ag-ZrO$_2$ nanoparticles. The EDX spectrum of EG/Ag-ZrO$_2$ (Figure 1d) demonstrates that the composite contains O, C, Ag, and Zr. The presence of these elements confirms that the EG/Ag-ZrO$_2$ composites have been successfully synthesised.
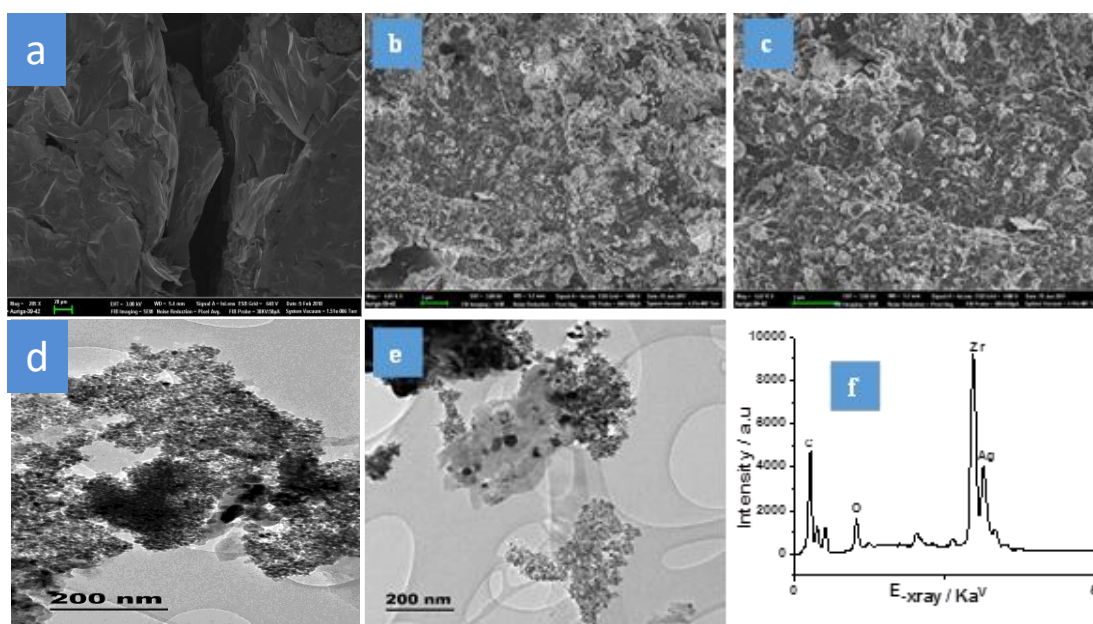
Figure 1. SEM Images of (a) EG, (b) EG/ZrO$_2$, (c) EG/Ag-ZrO$_2$, TEM images of (d) Ag-ZrO$_2$, (e) and (d) EG/Ag-ZrO$_2$ and (f) EDS of EG/Ag-ZrO$_2$

3.2 XRD analysis

Figure 2 represents the X-ray diffractograms of ZrO_2, EG-ZrO_2, and EG/Ag-ZrO_2 composites. The XRD pattern of ZrO_2 (Figure 2a) exhibits peaks at 2θ of 30.3°, 50.3°, and 60.2°, which correspond to (011), (112), and (121) reflection planes, respectively. The intensities and the positions of these peaks (Figure 2a) indicate that the synthesized nanocomposite is crystalline and exist in the tetragonal phase of ZrO_2 according to JCPDs card No. 50-1089 [34]. Apart from the identifiable peaks of pure ZrO_2, the EG-ZrO_2 (Figure 2b) and EG/Ag-ZrO_2 (Figure 2c) samples display additional peaks at $2\theta = 26.4°$ (002), 38.1° (100), 44.2° (101), 54.7° (004), 64.3° (110), and 77.3° (112), which represent peaks arising from EG [35]. No peak characteristic for Ag appears in the XRD spectrum as a result of the small concentration of Ag (0.5w %) when compared to that of ZrO_2 [36]. The average crystallite size of the nanocomposites was calculated to be 44 nm. These values were calculated based on the Debye–Scherrer equation (Equation 1) using the peaks with the highest intensities:

$$D = \frac{K\lambda}{\beta \cos\theta} \qquad\qquad\qquad (1)$$

Where D is the crystallite size, λ is the wavelength of the radiation (1.54 nm), K is shape factor (0.9), β is the full width at half maximum of the highest intensity peak, and θ is the Bragg angle of the most intense peak at a specific phase.
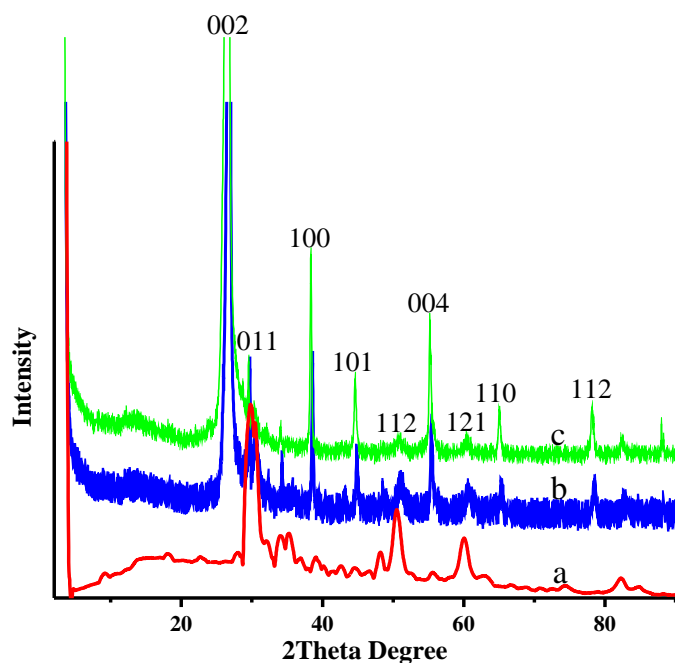
Figure 2. XRD patterns of (a) ZrO_2, (b) Ag-ZrO_2, and (c) EG/Ag-ZrO_2

3.3 Raman spectroscopy analysis

The tetragonal phase of zirconia has six Raman active modes [37]. The Raman spectrum of ZrO_2 (Figure 3a) displays Raman active modes that are unique to tetragonal ZrO_2. These bands appear at 186 cm^{-1}, 312 cm^{-1}, 374 cm^{-1}, 399 cm^{-1}, 644 cm^{-1}, and 729 cm^{-1} and correspond to the tetragonal Raman

vibrational modes of ZrO_2. Figure 3b represents Raman spectra of EG, EG/ZrO_2, and EG/Ag-ZrO_2 composites. Graphite displayed two exclusive Raman bands known as D (disorder) and G (graphitic) bands [38]. The peak at 1639 cm^{-1}, which is the G band, represents the scattering on E_{2g} phonon vibration of sp^2 bonded carbon atoms [39]. The D band of these samples (EG, EG/ZrO_2, and EG/Ag-ZrO_2) appears at 1533 cm^{-1}. The appearance of this peak specifies the presence of disorder in the hexagonal lattice of graphite, caused by internal structural defects and/or dangling bonds [38]. The comparatively high intensity of the G band in the EG/Ag-ZrO_2 composite indicates the existence of C–C sp^2 bonds, whereas the low intensity of the D band suggested that EG was not disrupted significantly by the incorporation of Ag-ZrO_2. The Raman spectroscopic analysis does not only support the successful fabrication of the EG/Ag-ZrO_2 electrode but corroborates also the results of XRD analysis, which showed that ZrO_2 is composed mainly of the tetragonal phase.
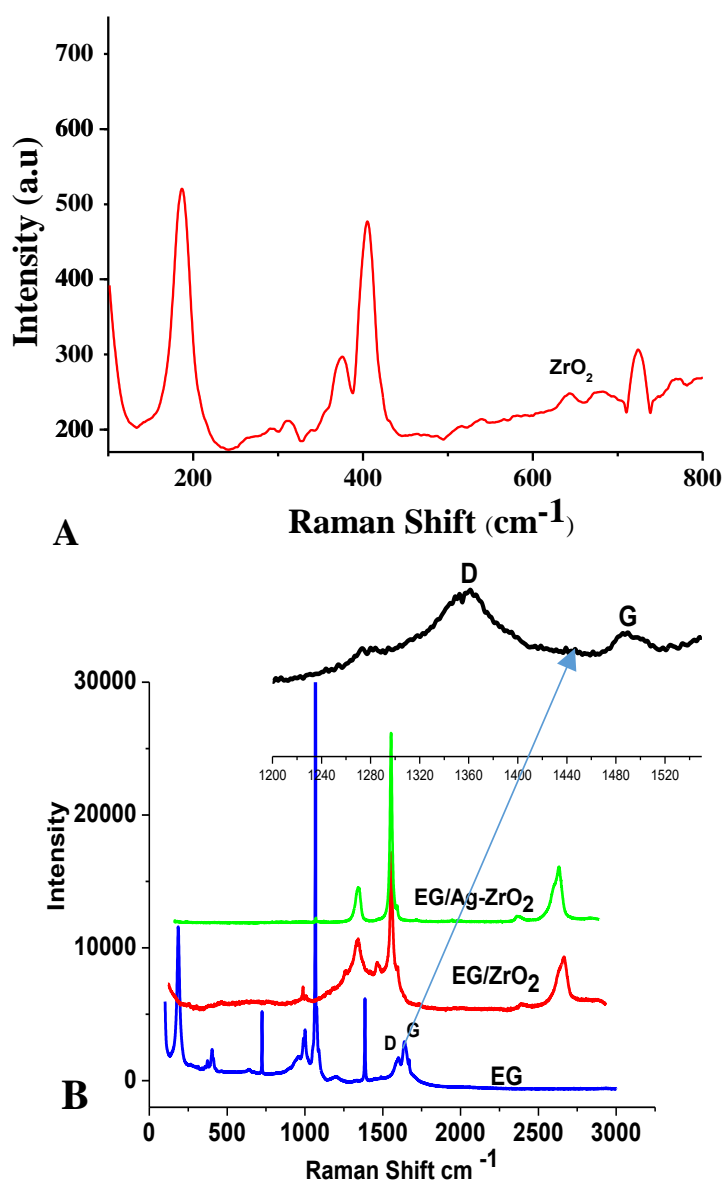
Figure 3. Raman spectra of ZrO_2, EG, EG-ZrO_2, and EG/Ag-ZrO_2

3.4 Thermogravimetric analysis (TGA)

TGA was executed to examine the thermal stabilities of the as-synthesized samples (Figure 4). The losses in weight observed in temperature ranges from about 10 °C to 200 °C for ZrO_2 sample (Figure 4a), and from about 50 °C to 100 °C for $EG-ZrO_2$ and $EG/Ag-ZrO_2$ samples (Figures 4b & 4c) are caused by the evaporation of water/moisture from the surfaces of the samples. The slight weight loss observed from 100 °C to about 380 °C for all the samples is attributed to active pyrolysis. The significant weight loss detected for all samples in the 380–900 °C range is attributed to the decomposition of EG in the composites.
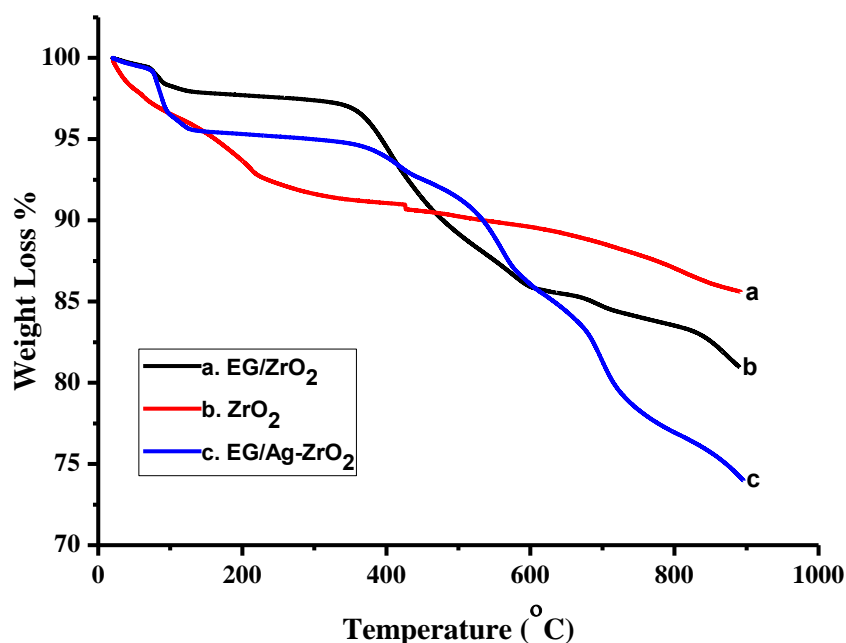
Figure 4. TGA plots of (a) ZrO_2, (b) EG/ZrO_2, and (c) $EG/Ag-ZrO_2$

3.5 Fourier transforms infrared spectroscopy analysis

The presence and nature of different functional groups in the nanocomposite samples were determined using Fourier transform infrared (FTIR) spectroscopy (Figure 5). For all the samples, all peaks observed below 100 cm^{-1} were accredited to Zr–O bonding. The FTIR peak appearing at around 1380 cm^{-1} is allocated to O–H bonding, while the peak at 1553 cm^{-1} is associated with adsorbed moisture on the surface of the nanocomposites. The appearance of the peak between 3425 and 3445 cm^{-1} confirms the presence of hydroxyl groups [40]. The peaks characteristic for C=O stretching vibrations in EG are observed at around 1720 cm^{-1}. Other peaks arising from EG appear at 500 cm^{-1}, 1060 cm^{-1}, and 2400 cm^{-1} and correspond to C=C bending vibrations, C–O stretching vibrations, and CH_2 stretching and deformation vibrations, respectively [41]. The peak located at about 2950 cm^{-1} represents the C–H group.
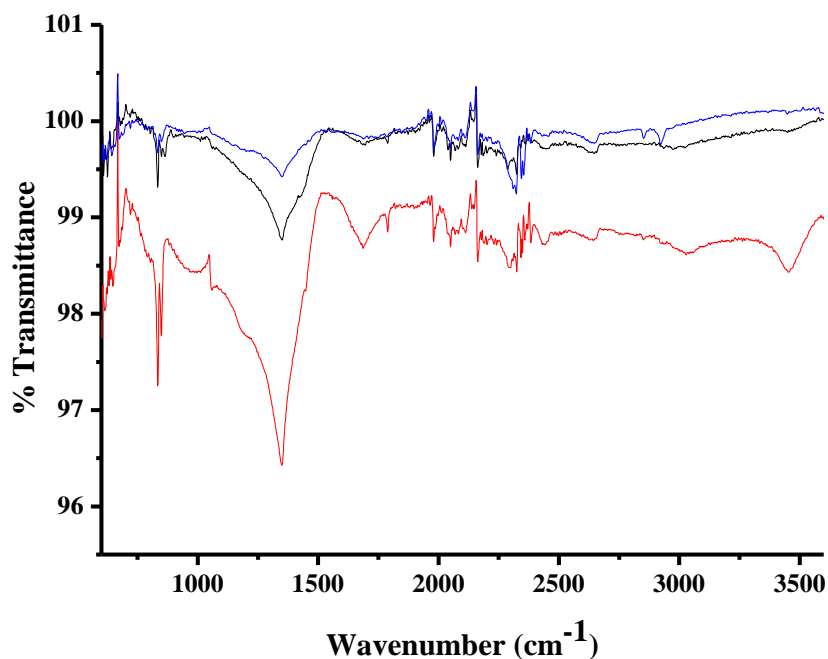
Figure 5. FTIR spectra of (a) ZrO_2, (b) EG/ZrO_2, and (c) $EG/Ag-ZrO_2$

3.6 Optical analysis
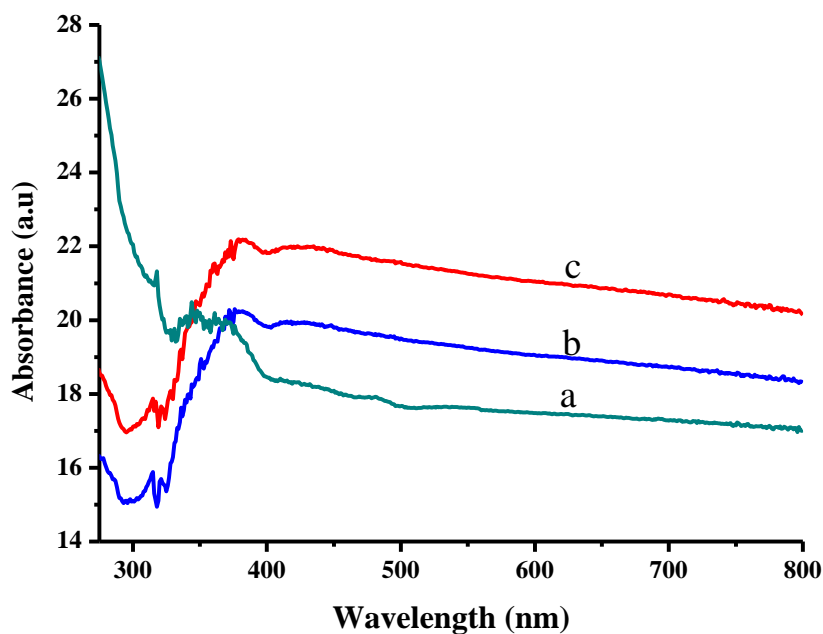
Figure 6. UV-Vis absorption spectra of (a) ZrO_2 (b) EG/ZrO_2, and (c) $EG/Ag-ZrO_2$

The samples' visible light activities were probed using UV-Vis spectroscopy. The UV-Vis absorption spectra of the samples (Figure 6) revealed that the visible light absorptivity of ZrO_2 was enhanced by the introduction of EG. Thus, the EG/ZrO_2 demonstrated higher visible light absorption ability than pure ZrO_2. A further increase in the visible light absorption of ZrO_2 occurred with the introduction of Ag. Thus, the increased visible light activity of the $EG/Ag-ZrO_2$ electrode is caused by

the synergistic effects of both Ag and EG presence of Ag most likely leads to the creation of impurities in the intrinsic bands, causing thus a change in the optical band gap of ZrO_2. By contrast, the EG behaved as a photosensitizer to improve the light absorption of the sample in the visible light region. High visible light activity implies enhanced pollutant degradation ability [24]. The EG/Ag-ZrO_2 electrode, which exhibits the highest visible light activity, is expected therefore to demonstrate the highest efficiency in the degradation of the pollutants.

The band gaps of the synthesized electrodes were calculated using the Kubelka–Munk Equation 2:

$$F(R) = \frac{(1-R)}{2R} \qquad\qquad (2)$$

which was obtained from the diffuse reflectance data. The reflectance (R) is equal to $R_{sample}/R_{reference.}$ The Kubelka–Munk equation was used to construct a Tauc plot ((([F(R)*hv]^n vs. photo energy (hv)), where n is an integer and its value is dependent on the nature of the semiconductor used. The Tauc plots for the three materials synthesized in the present study are depicted in Figure 7. The band gaps were calculated through extrapolation of the Kubelka–Munk function to $F(R) = 0$. The results show a reduction in the band gap of ZrO_2 upon introduction of EG and a further reduction caused by the incorporation of Ag as a dopant. Thus, the presence of EG and Ag facilitates a reduction in ZrO_2 band gap, which in turn produces an improvement in the photoactivity observed. The results of this analysis corroborate the outcomes determined using UV-Vis absorption spectroscopy analysis.
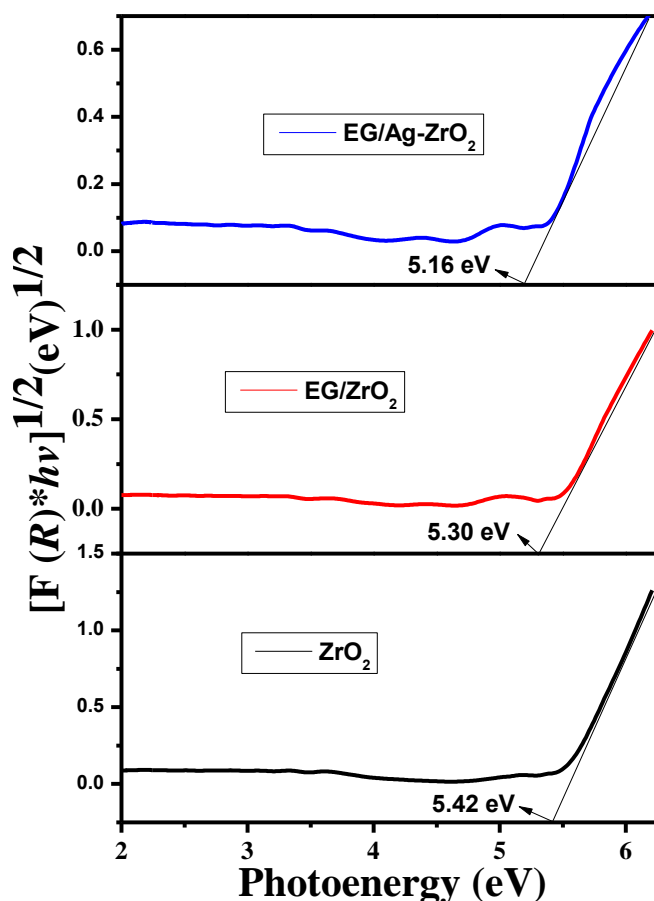
Figure 7. Tauc plots for (a) ZrO_2 (b) EG/ZrO_2, and (c) EG/Ag-ZrO_2

3.7 Brunauer–Emmett–Teller (BET) analysis

BET surface area analysis was aimed at determining the surface areas and pore volumes of the synthesized electrodes. Typically, catalysts possessing large surface areas and pore volumes display enhanced capacity to adsorb a variety of organic pollutants onto their surfaces, facilitating improved photoelectrochemical degradation of the pollutants. The results of the BET analysis of the EG, EG/ZrO$_2$, and EG/Ag-ZrO$_2$ electrodes (Table 1) show that all the electrodes possess large surface areas, and pore volumes with EG/Ag-ZrO$_2$ exhibiting the highest surface area (16.99 m^2 g^{-1}) and pore volume (0.07996 cm^3 g^{-1}). All of the prepared electrodes are therefore expected to exhibit high pollutant degradation efficiencies, with EG/Ag-ZrO$_2$ potentially showing the highest efficiency.

Table 1. BET data obtained for EG, ZrO$_2$, Ag-ZrO$_2$, and EG/Ag-ZrO$_2$

Sample	BET surface area (m^2 g^{-1})	Pore volume (cm^3 g^{-1})
EG	11. 98	0. 03697
ZrO$_2$	15.67	0. 06992
EG/ZrO$_2$	16.42	0. 07868
EG/Ag-ZrO$_2$	16.99	0. 07996

3.8 Electrochemical characterization of EG and EG/Ag-ZrO$_2$ electrodes

Figure 8(i) shows the cyclic voltammograms of EG and EG/Ag-ZrO$_2$ electrodes. The voltammograms were acquired using a 10-mM potassium ferricyanide ([Fe(CN)$_6$]$^{-3/-4}$) solution to probe the electrochemical potentials of the fabricated electrodes at 20 mV s^{-1}. Comparatively, the EG/Ag-ZrO$_2$ electrode displayed a higher current than the EG electrode as a result of the larger specific surface area of the EG/Ag-ZrO$_2$ caused by the presence of ZrO$_2$ nanoparticles in the composite.

The electrochemical impedance spectroscopy (EIS) measurements (Figure 8 (ii)) was conducted to characterize the charge transfer resistance (Rct) between the electrolyte and interfaces of EG, Ag-ZrO$_2$, and EG/Ag-ZrO$_2$ electrodes. The open circuit potential (0.0 V) and at the frequency range of 0.1-100 kΩ were used in this measurement. As can be seen in Figure 8(ii), particularly at a higher frequency, the semicircle for EG/Ag-ZrO$_2$ shows lower semicircle arc radius than those of EG and Ag-ZrO$_2$ semicircles. This observation is attributed to predominant electron transport property and ionic conduction at the interface between the EG/Ag-ZrO$_2$ electrode and the electrolyte [42, 43]. Furthermore, in the fitting of the EIS data using an electrical equivalent circuit (EEC) shown in Figure 8 (iii), the calculated Rct values were 834.3 Ω, 539.2 Ω and 115.1 Ω for EG, Ag-ZrO$_2$, and EG/Ag-ZrO$_2$, respectively. The suppression of Rct observed when EG is incorporated to Ag-ZrO$_2$ shows an ideal photoanode which provides efficient photoelectrochemical process. Furthermore, both bode modulus

and phase plots which are shown in Figure 8 (iii) and (iv) also corroborate the Nyquist diagrams as the impedance and phase angles at the region pin-pointing Rct behaviour (at low-frequency range) are low for EG/Ag-ZrO$_2$. All these show a better separation rate of electrons and holes leading to a relatively efficient Rct ideal for good photoelectrochemical processes at the electrolyte and electrode interface [44, 45].
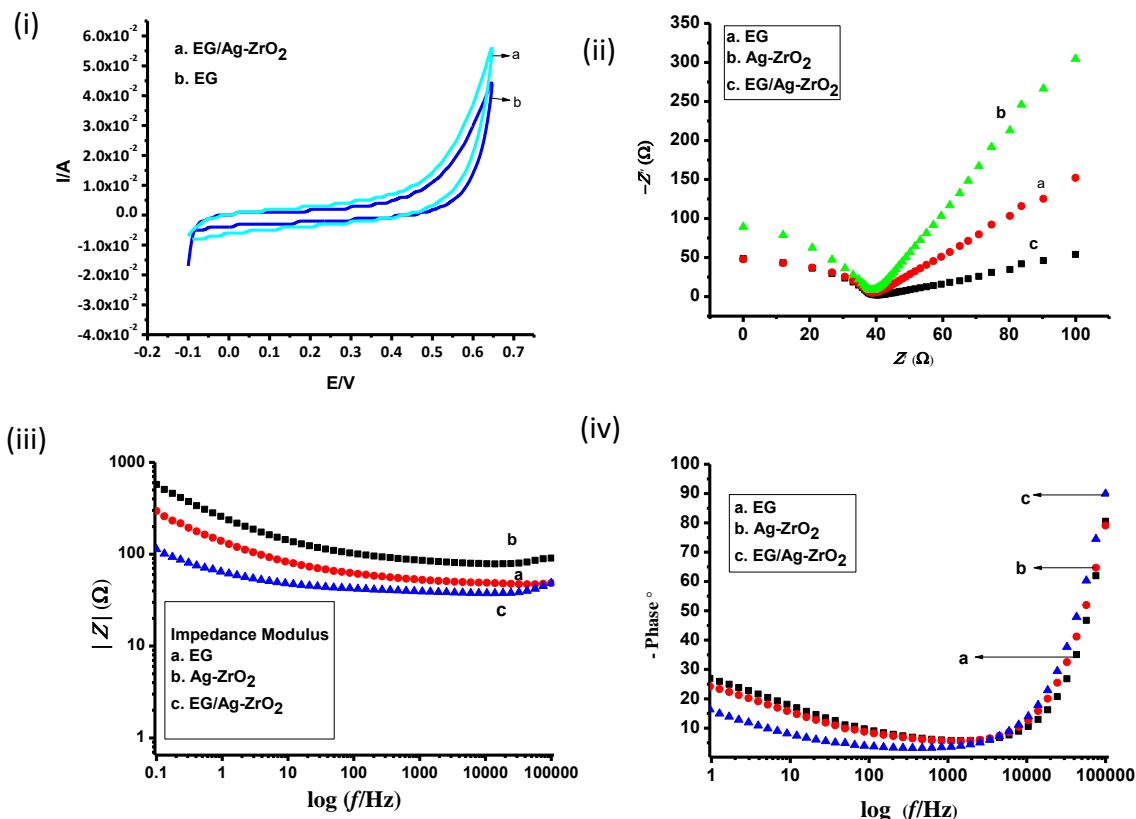
Figure 8. Figure 8 (i) Cyclic voltammogram (ii) Nyquist diagrams (ii) (iii) impedance modulus and (iv) phase plot of EG, Ag-ZrO$_2$ and EG/Ag-ZrO$_2$ electrodes.

3.9 Photoelectrochemical degradation studies

The capacities of the fabricated electrodes (EG, EG-ZrO$_2$, and EG/Ag-ZrO$_2$) to photoelectrochemically degrade organic pollutants in water were determined by the application of the electrodes to the degradation of MB (100 mL, 20 mg/L) under visible light irradiation. The degradation experiments were first conducted in order to identify the most efficient catalyst. Once identified, the performance of the most efficient catalyst was optimized by examining the efficiency of the dye degradation process as a function of pH, current density, and voltage.

3.9.1 Effect of catalyst modification

The photoelectrochemical degradation profiles of MB dye obtained using the EG, EG/ZrO$_2$, and EG/Ag-ZrO$_2$ electrodes are depicted in Figure 9a.
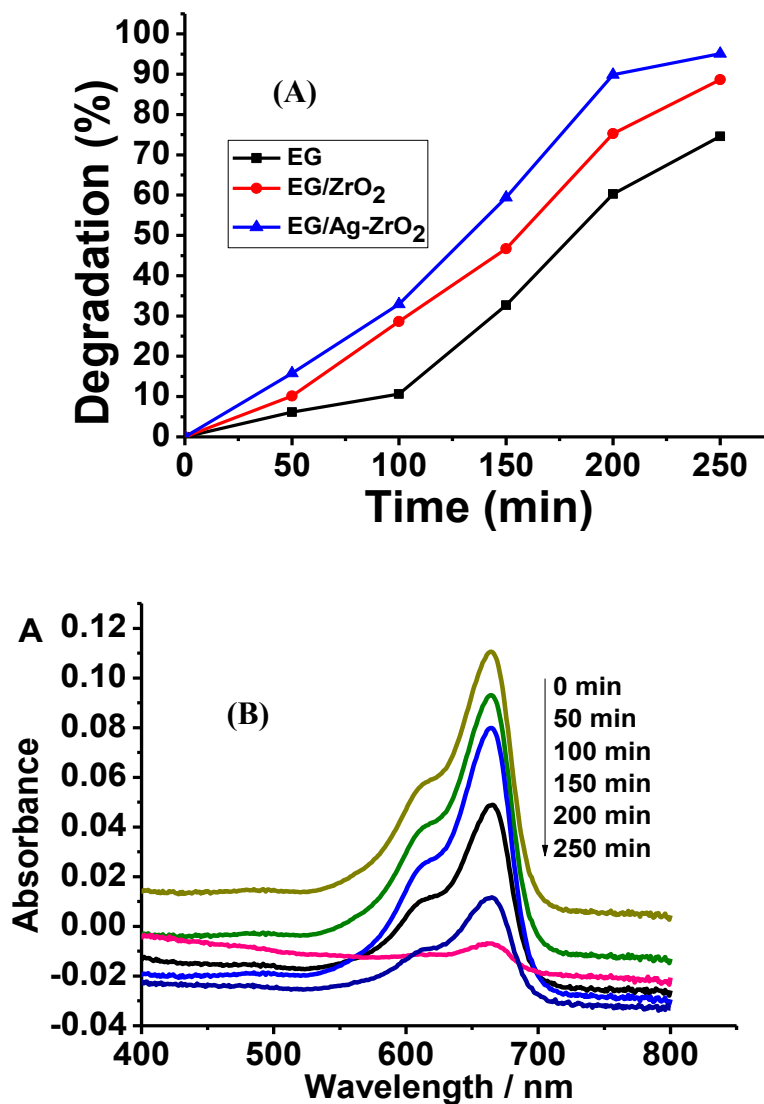
Figure 9. Methylene blue degradation profiles observed in the presence of (A) EG, EG-ZrO$_2$, and EG/Ag-ZrO$_2$ electrodes and (B) EG/Ag-ZrO$_2$ electrode, at current and voltage ranges of 7.5–15 mA and 1–3 V, respectively

The results showed that the degradation efficiencies of the electrodes toward MB were in the following order: EG < EG-ZrO$_2$ < EG/Ag-ZrO$_2$. Thus, the modification of EG with ZrO$_2$ and Ag improved the MB degradation efficiency of the electrode, and EG/Ag-ZrO$_2$ afforded the most efficient electrode with about 99.7% efficiency owing to the synergistic effects of Ag and ZrO$_2$ incorporation. Doping of metal oxides with Ag has been shown to enhance both optical and electrical characteristics of

catalysts [46]. Meanwhile, EG is known to improve the optical activity of catalysts by acting as a photosensitizer [24]. In addition, EG can also reduce the electron-hole recombination rate, and increase the surface area of the electrode for enhanced pollutant adsorption. Figure 9b further ascertains the appropriateness of the EG/Ag-ZrO$_2$ for the degradation of MB at the voltage and current ranges of 1–3 V and 7.5–15 mA. The gradual reductions in the intensities of the peaks characteristic for MB at 609 nm and 668 nm over time confirm the gradual degradation of the dye. This result is comparable to that obtained by Feng et al [47] where Ag doping enhanced the visible light and photocatalytic activities of ZnO mesoporous nanowall arrays (MNWAs).

3.9.2 Effect of pH on the photoelectrochemical degradation of MB

The solution pH is an important factor that needs to be considered during the photoelectrochemical degradation of dyes in wastewater solutions. Specifically, the pH determines the surface charge characteristics of the metal oxide catalysts, which in turn influences the effectiveness of the degradation process. In this study, the pH was varied from 2 to 11 and its effect on the rate of the degradation of MB by the EG/Ag-ZrO$_2$ electrode (Figure 10) was examined. The dye degradation efficiency increased with increasing pH, and the highest and lowest efficiencies were detected at a pH of 11 and 2, respectively.
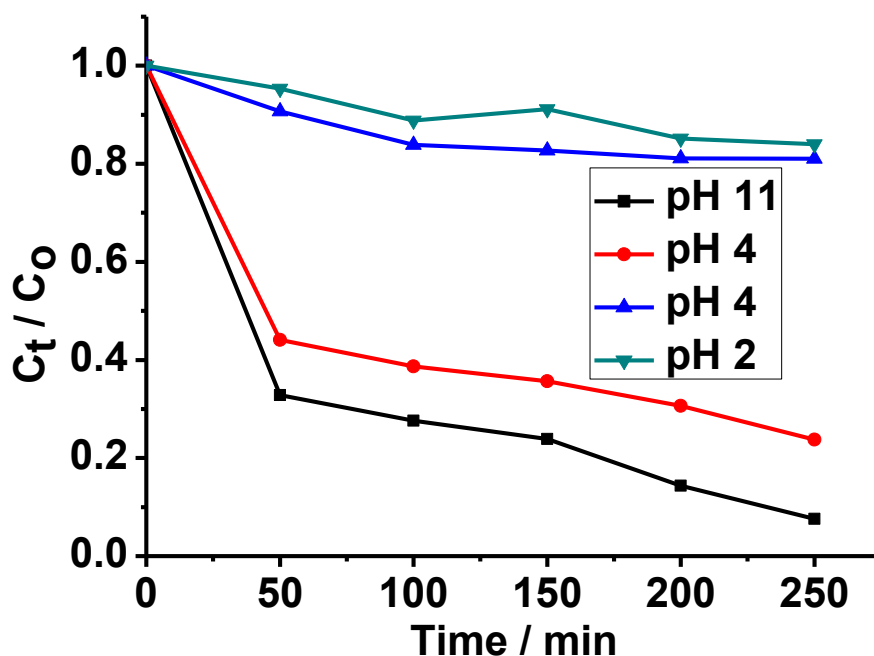
Figure 10. Effect of pH on the photoelectrochemical degradation of 20 mg/L solution of methylene blue dye by EG/Ag-ZrO$_2$ at current and voltage ranges of 7.5–15 mA and 1–3 V, respectively

The pH-dependency of the MB degradation process can be explained in terms of the surface charges in acidic and basic media. The surface of the electrode becomes negatively charged at higher pH values (basic medium) as a result of the accumulation of OH$^-$ ions on the electrode surface [48].

Meanwhile, according to literature [49], the aqueous solution of MB is positively charged. There is, therefore, an electrostatic attraction between the negatively charged EG/Ag-ZrO$_2$ electrode surface and the positively charged methylene blue dye. This attraction leads to enhanced adsorption of dye molecules on the electrode surface, which is a necessary pre-requisite for efficient photoelectrochemical degradation. The enhanced absorption explains the high degradation efficiency in the basic medium. By contrast, the surface of the electrode becomes positively charged at low pH values (acidic medium) as a result of the presence of H$^+$ ions on its surface. The positively charged electrode surface repels the positively charged dye molecules, causing them to be sparingly adsorbed onto the electrode, and resulting in low degradation efficiency.

3.9.3 Effect of current density on the photoelectrochemical degradation of MB

Figure 11 shows the relationship between current density and MB concentration decay. An improvement in the dye removal efficiency was realised upon increasing the density of the current from $2 \, mA \, m^{-2}$ to $10 \, mA \, m^{-2}$. The increase in the current density increases the frequency of electron excitation from the valence band to the conduction band of ZrO$_2$ upon light irradiation. This increase leads subsequently to the generation of a higher number of holes and reactive oxygen species, as well as HO• radicals, all of which are excellent oxidizing agents, and enhance thus the degradation rate.
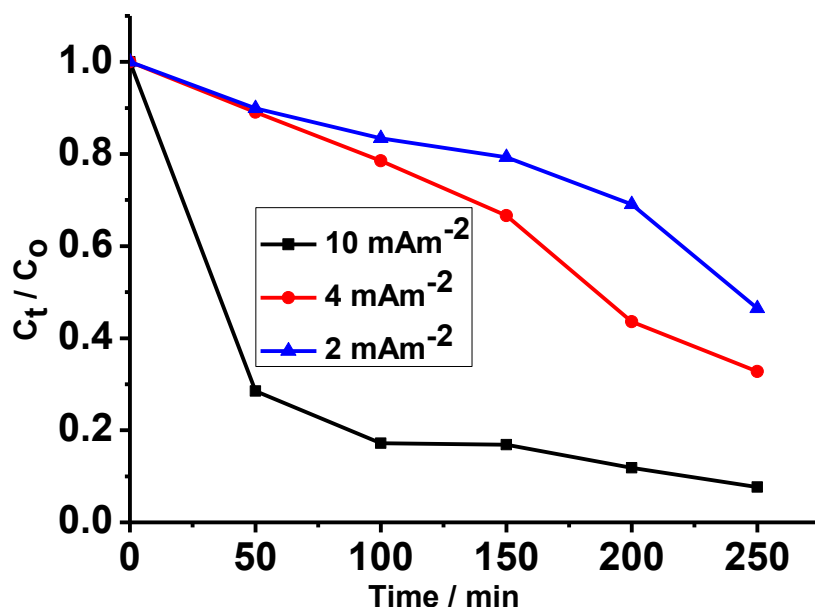
Figure 11. Effect of current density on the photoelectrochemical degradation of 20 mg/L solution of methylene blue at pH 11 by EG/Ag-ZrO$_2$ in a voltage range of 1–3 V

3.9.4 Effect of potential on the photoelectrochemical degradation of MB

The relationship between applied potential and MB degradation efficiency of the EG/Ag-ZrO$_2$ electrode is displayed in Figure 12. The results showed that a direct relationship between the dye

degradation efficiency and the applied potential exists. This relationship is caused by the effective separation of the photogenerated electrons and holes as a result of the external photoanode electric field. An increase in the applied potential causes enhanced separation of charge carriers, which in turn results in the generation of high concentration of OH radicals in the solution. From the present results, the applied potential of 2 V was found to be optimal, affording a degradation efficiency of 93%.
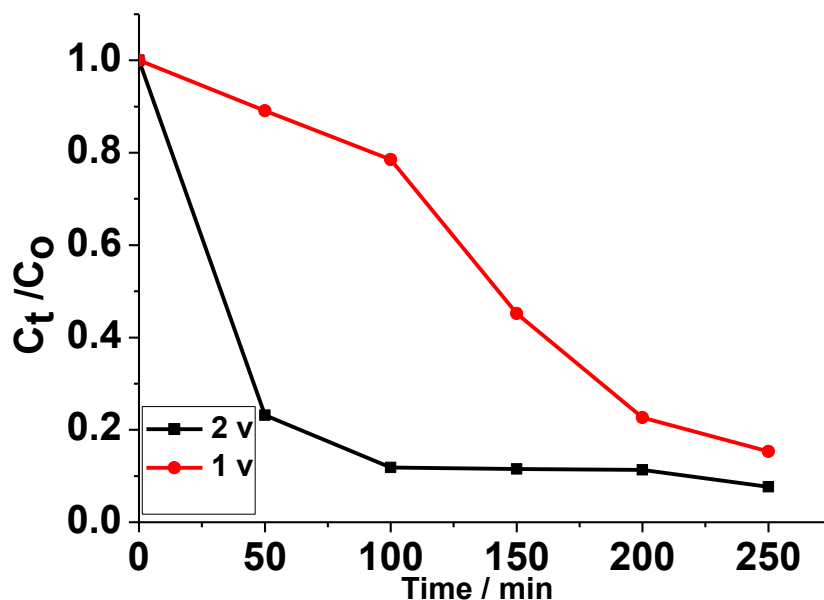
Figure 12. Effect of voltage on the photoelectrochemical degradation of 20 mg/L solution of methylene blue dye by EG/Ag-ZrO$_2$ at pH 11 and current of 10 mA m^{-2}

3.10 Photolysis, electrochemical, and photoelectrochemical degradation studies

The EG/Ag-ZrO$_2$ was applied to the degradation of MB electrochemical and photoelectrochemical methods, and the results, together with those obtained via simple photolysis, are compared in Figure 13. The photolysis procedure was performed with visible light only, i.e., no electrode was employed. The electrochemical degradation was executed with the electrode in the absence of light, and the photoelectrochemical degradation was carried out with the electrode in the presence of light. The result demonstrated the superiority of the photoelectrochemical process for the degradation of MB over both photolysis and the electrochemical method. These results confirm that the efficiency of the MB degradation process is highest in the presence of both visible light and the EG/Ag-ZrO$_2$ electrode.

The kinetics of the MB dye degradation by electrodes under the various conditions were studied using pseudo-first-order reaction kinetics (eqn 2).

$$\frac{\ln C_o}{C_t} = kt \qquad (2)$$

where C_o and C_t represent the initial dye concentration and the dye concentration at time t respectively, while k represents the first-order rate constant.

Notable linear fits were detected for all the electrodes (EG, EG/ZrO$_2$, and EG/Ag-ZrO$_2$). The rate constant values (Table 2) for the three electrodes under photoelectrochemical degradation are present in

the following order: EG< EG/ZrO₂< EG/Ag-ZrO₂, indicating that the EG/Ag-ZrO₂ degraded the dye at the fastest rate. The rate of degradation of the dye with the EG/Ag-ZrO₂ electrode is also faster under photoelectrochemical degradation compared to electrochemical and photolysis.
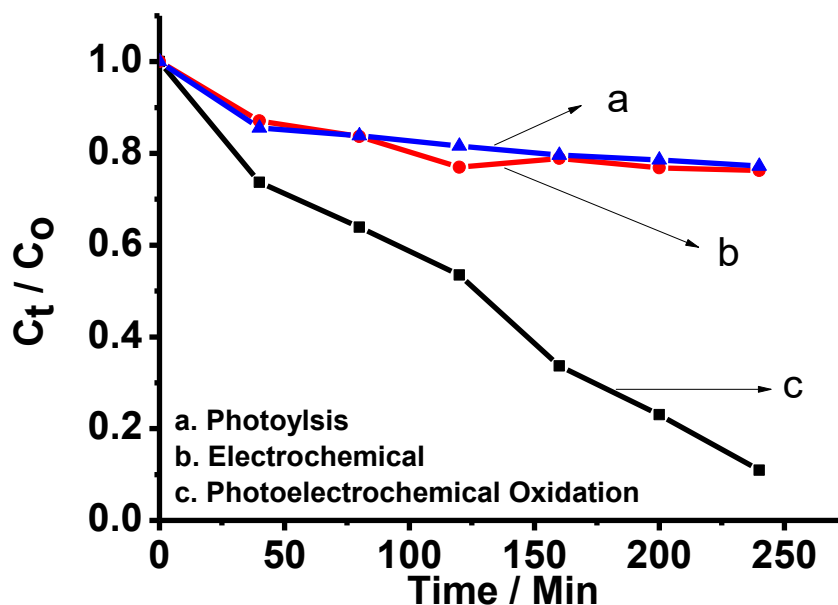
Figure 13. Normalized concentration decay curves obtained during the (a) photolysis (+ light, no electrode), (b) electrochemical (no light, + electrode), and (c) photoelectrochemical degradation (+ light and electrode) of 20 mg/L solution of methylene blue dye. The electrode was comprised of EG/Ag-ZrO₂

3.11 comparison of the effectiveness of the as-synthesized electrode (EG/Ag-ZrO₂) with other published results of EG-based electrodes

In order to ascertain its superiority over other EG based electrodes, the efficiency of the as-synthesized EG/Ag-ZrO₂ electrode has been matched with other published data involving different EG based electrodes (Table 3). The result evidenced that the EG/Ag-ZrO₂ is an effective electrode as it showed a much higher degradation efficiency in comparison to the other EG based electrodes used.

Table 2. Rate constant values for MB degradation

Sample	K (min^{-1})
EG (photoelectrochemical)	0.2736
EG/ZrO₂ (photoelectrochemical)	0.9825
EG/Ag-ZrO₂ (a) photoelectrochemical	2.9427
(b) electrochemical	0.0481
(c) photolysis	0.0320

Table 3. Comparison of the effectiveness of different EG based electrodes

Names of catalysts	Dyes used	% degradation	References
EG-diamond	Anthraquinone	81	[50]
EG/Se-ZnO	Methylene blue	98.5	[51]
EG-ZnO	Methylene blue	96	[52]
EG-TiO$_2$	Methylene blue	85	[53]
EG-WO$_3$	Orange II	82	[54]
EG/Ag-ZrO$_2$	Methylene blue	98.8	[This work]

3.11 HPLC analysis

HPLC analysis was performed to identify the by-products of MB formed during its photoelectrochemical degradation mediated by EG/Ag-ZrO$_2$ (Figure 14A). As shown by UV-Vis analysis (Figure 14B), the concentration of MB decreased with increasing time (monitored at 668 nm). This decrease was accompanied by the appearance of new peaks in the HPLC chromatogram (Figure 14A), which indicates significant destruction of the MB dye and the formation of different by-products. Five peaks assigned to MB, and the intermediate products (Azura B, Azura A, Azura C, and Thoinin), with retention times of 15.6, 9.3, 8.1, 6.7, and 5.6 min, respectively, are observed. Peaks with similar retention times were previously observed for the same dyes by Rauf et al. [55].
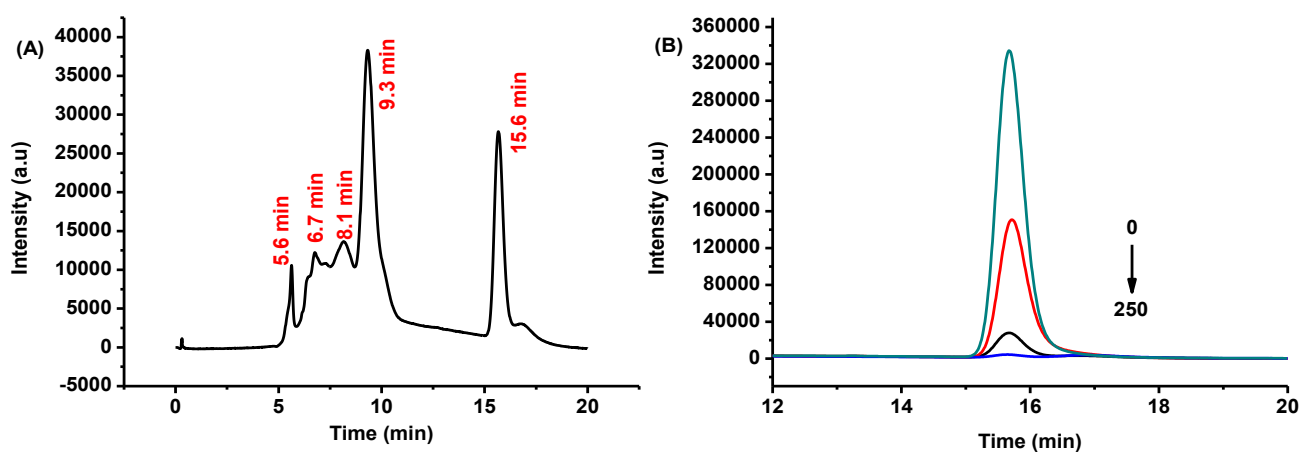
Figure 14. (A) UV-Vis spectrum and (B) HPLC chromatograms of methylene blue photoelectrochemical degradation by EG/Ag-ZrO$_2$ obtained at a wavelength of 668 nm.

4. CONCLUSIONS

Electrodes comprised of EG, EG-ZrO$_2$, and EG/Ag-ZrO$_2$ have been successfully synthesized in this study, as evidenced by the results of FTIR spectroscopy and EDX analyses. The SEM revealed that in the images of EG-ZrO$_2$ and EG/Ag-ZrO$_2$ electrodes, ruptured EG is evenly covered by ZrO$_2$ and Ag-ZrO$_2$ nanoparticles, respectively. The XRD and Raman spectroscopy analyses showed that ZrO$_2$ exists

in the tetragonal phase. The visible light activity of EG was improved by the introduction of Ag and EG, and EG/Ag-ZrO$_2$ was identified as the most effective electrode for the degradation of MB. In contrast to photolysis and photocatalytic degradation, which exhibited minimal degradation efficiencies, the photoelectrochemical method resulted in significant degradation of MB. The high efficiency of the EG/Ag-ZrO$_2$ electrode toward the degradation of MB is attributed to the synergistic effects of Ag and EG, which enhance the photocatalytic performance of the electrode by improving its visible light absorption and increase its pollutant adsorption capacity by increasing the specific surface area.

References

1. H. Chaudhuri, S. Dash, A. Sarkar, *J of Porous Mater.*, 23 (2016) 1227-1237.
2. A. Slampova, D. Smela, A. Vondrackova, I. Jancarova, V. Kuban, *Feedback.*, 91 (1997)
3. U.G Akpan, B.H Hameed, *J Hazard Mater.*, 170(2009) 520-529.
4. X. Li, D. Pletcher, F.C Walsh, *Chem Soci Rev.*, 40 (2011) 3879-3894.
5. D. Ravelli, D. Dondi, M. Fagnoni, A. Albini, *Chem Soci Rev.*, 38 (2009)1999-2011.
6. J.S. Bae, H.S Freeman, *Dyes Pigm.*, 73 (2007) 81-85.
7. L.S. Andrade, T.T. Tasso, D.L da Silva, R.C Rocha Filho, N. Bocchi, S.R Biaggio *Electrochim Acta.,* 54 (2009) 2024-2030.
8. J.H. Jou, Y.X. Lin, S.H. Peng, C.J Li, Y.M Yang, C.L. Chin, M.C. Liu *Adv Funct Mater.*, 24 (2014) 555-562.
9. M. Muruganandham, M. Swaminathan., *Dyes Pigm,* 62(2004) 269-275.
10. F. Han, V.S.R. Kambala, M. Srinivasan, D. Rajarathnam, R. Naidu., *Appl Catal A-Gen* 359 (2009) 25-40.
11. U.G. Akpan, B.H. Hameed., *J Hazard Mater* 170 (2009) 520-529.
12. M. Zhou, J. He., *J. Hazard Mater* 153 (2008) 357-363.
13. M. Panizza, G. Cerisola, *J Hazard Mater.*, 153 (2008) 83-88.
14. M.T. Fukunaga, J.R. Guimarães, R. Bertazzoli, *Chem Eng J.,* 136 (2008) 236-241.
15. M. Harikishore, M. Sandhyarani, K. Venkateswarlu, T.A. Nellaippan, N. Rameshbabu, *Procedia Mater Sci.,* 6 (2014) 557-566.
16. A. Hassanvand, M. Sohrabi, S.J. Royaee, M. Jafarikajour, *Adv Mater Res.*, 875 (2014) 28-33
17. M. Zhang, C. Chen, Ma W, J. Zhao, *Angew Chem.*, 120 (2008) 9876-9879.
18. E. Casbeer, V.K. Sharma, X.Z. Li, a review. *Sep. Purif. Technol.*, 87 (2012) 1-14.
19. L.J.J. Janssen, L. Koene, *Chem Eng J* 85 (2002) 137-146.
20. L. Fan, Y. Zhou, W. Yang, G. Chen, F. Yang, *Dyes Pig.*, 76 (2008) 440-446.
21. B.K. Körbahti, S. Taşyürek, *Desalin Water Treat.*, 57 (2016) 2522-2533.
22. H.S. Kang, B.D. Ahn, J.H. Kim, G.H. Kim, S.H. Lim, H.W. Chang, S.Y. Lee, *Appl Phy Lett.*, 88 (2006) 202108.
23. L. Shi, L.H. Reid, W.D. Jones, R. Shippy, J.A. Warrington, S.C. Baker, Y. Luo, *Nature Biotechnol.*, 24 (2006) 1151.
24. O.M. Ama, N. Mabuba, O.A. Arotiba, *Electrocatalysis.*, 6 (2015) 390-397.
25. F. Zhang, Q. Zhao, X. Yan, H. Li, P. Zhang, L. Wang, L. Ding, *Food Chem.*, 197 (2016) 943-949.

26. T. Ndlovu, O.A. Arotiba, S. Sampath, R.W. Krause, B.B. Mamba, *J Appl Electrochem*., 41 (2011) 1389-1396.
27. C.A. Martinez-Huitle, S. Ferro, *Chem Soci Rev*., 35 (2006) 1324-1340.
28. M. Mazur,*Electrochem Commun*., 6 (2004) 400-403.
29. I. Capek, *Adv. Colloid Interface Sci*., 110 (2004) 49-74.
30. C.M. Fan, B. Hua, Y. Wang, Z.H. Liang, X.G. Hao, S.B. Liu, Y.P. Sun *Desalination*., 249 (2009) 736-741.
31. M. Tian, B. Adams, J. Wen, R.M. Asmussen, A. Chen, *Electrochim Acta*., 54 (2009) 3799-3805.
32. M. Tian, B. Adams, J. Wen, R.M. Asmussen, A. Chen, *Electrochim Acta,* 54 (2009) 3799-3805.
33. R.T. Pelegrini, R.S. Freire, N. Duran, R. Bertazzoli, *Environ Sci Technol*., 35 (2001) 2849-2853.
34. W.W. Anku, S.O.B. Oppong, S.K. Shukla, E.S. Agorku, P.P. Govender, *Nat Sci-Mater.,* 26 (2016) Pro 354-361.
35. M. Epifani, C. Giannini, L. Tapfer, L. Vasanelli, *J Am Ceram Soc*., 83 (2000) 2385-2393.
36. H.M. Yates, L.A. Brook, I.B. Ditta, P. Evans, H.A. Foster, D.W. Sheel, A. *Steele J Photochem Photobiol A Chem.,* 197 (2008) 197-205.
37. W.W. Anku, S.O.B. Oppong, S.K. Shukla, E.S. Agorku, P.P. Govender, *Pro Nat Sci-Mater*., 26 (2016) 354-361.
38. I.M. Clegg, N.J. Everall, B. King, Melvin H, C. Norton, *Appl. Spectrosc*., 55 (2001) 1138-1150.
39. B. Debelak, K. Lafdi, *Carbon*., 45 (2007) 1727-1734.
40. S. Rani, S. Verma, S. Kumar *Appl Phys A.,* (2017) 123: 539.
41. S.N. Alam, L. Kumar, N. Sharma, *Graphene*., 4 (2015) 91.
42. X. Hao, Y. Quansheng, S. Dan., Y. Honghui, L. Jidong, F. Jiangtao, Y. Wei, *J. Hazard. Mater*., 286 (2015) 509-516.
43. Y.C. Yen, C.C. Lin, P.Y.Chen, W.Y. Ko, T.R. Tien, K.J. Lin, *Royal Soc. Open Sci*., 4 (2017) 161051.
44. Y. Zhou, W. Fang, Y. Deng, L. Pan, B. Shen, H. Li, J. Zhang, *RSC Adv,* 7 (2017) 55927-55934.
45. C. Wang, F. Wang, M. Xu, C. Zhu, W. Fang, Y. Wei, *J Electroanal Chem*., 759(2015) 158-166.
46. S.N. Alam, L. Kumar, N. Sharma, *Graphene*., 4 (2015) 91.
47. Y. Feng, G. Wang, J. Liao, W. Li, C. Chen, M. Li, Z. Li, *Sci Rep,* 7 (2017) 11622.
48. H.S. Kang, B.D. Ahn, J.H. Kim, G.H. Kim, S.H. Lim, H.W. Chang, S.Y. Lee, *Appl Phys Lett*., 88 (2006) 202108.
49. T. Santhi, S. Manonmani, *Sustain Environ Res*., 22 (2012) 45-51.
50. M.G. Peleyeju, E.H. Umukoro, J.O. Babalola, O.A. Arotiba, *Electrocatalysis* 2 (2016) 132–139.
51. S.O. Idowu, M.G. Peleyeju, F.O. Oladoyinbo, O. Adejare, A.A. Tajudeen, A.A. Hameed, A.A. Omotayo, E.O. Dare, *J Nanoanalysis*., 4 (2017) 41-47.
52. O.M. Ama, O.A. Arotiba, *Int J Nano Med Eng.,* 2 (2017) 145-151.
53. O.M. Ama, O.A. Arotiba, *J. Electroanal. Chem*., 803 (2017) 157-164.
54. E.H.Umukoro, G.M. Peleyeju, C.J. Ngila, O.A. Arotiba, *Chem. Eng. J.* 317 (2017) 290–301.
55. G.W. Smith, T. Salman, *Can Metall Quart*., 5 (1966) 93-107.